Immobilised TiO_2 Mesocrystals with Exposed {001} Facets for Efficient Dye-Sensitized Solar Cells

Solar RRL
www.solar-rrl.com

Immobilised TiO_2 Mesocrystals with Exposed {001} Facets for Efficient Dye-Sensitized Solar Cells

*Bingyu Lei and Neil Robertson**

The immobilization of titanium dioxide is necessary for several energy and environmental applications such as dye-sensitized solar cells (DSSCs). A two-step fabrication route has been developed in this work including a near room temperature hydrolysis reaction to produce immobilized $(NH_4)_2TiOF_4$ arrays, followed by successive topotactic transformations to immobilised TiO_2 mesocrystals (im$cTiO_2$). Hierarchical mesocrystal structure has thereby been successfully introduced to immobilised TiO_2 without the use of expensive equipment or complex strategies. Thanks to the features of the nano-building blocks such as high surface area and high active {001} facets; collective properties including the common orientation of nanoparticles; and strong adhesion to the substrate inherited from the immobilized $(NH_4)_2TiOF_4$ precursor, the im$cTiO_2$ possesses a high dye pickup capability and optimal electron transport ability. The average power conversion efficiency from im$cTiO_2$ based DSSCs is comparable to devices with two layers of printed commercial TiO_2 under the same sintering condition, with the balanced short circuit current densities, similar open-circuit voltages, and outstanding fill factors.

1. Introduction

Titanium dioxide (TiO_2) has wide applications in various areas such as solar cells, energy storage and environmental purification because of its unique electronic, optical and catalytic properties and its long-term photostability.[1–4] A large number of investigations have focused on immobilization of TiO_2 since it is required for electrodes and is beneficial to catalyst separation in photocatalytic applications. For example, to work as the photoanode for dye-sensitized solar cells (DSSCs), powder form TiO_2 nanoparticles can be immobilised on transparent conductive oxide (TCO) substrates using different printing or coating techniques. The pre-formed nanoparticles or colloids need to be mixed well with additional chemicals to form a printable suspension or paste.[5,6] Alternatively, TiO_2 thin films can be directly deposited on substrates via sputtering,[7] chemical vapour deposition,[8] anodization,[9] dip-coating,[10] liquid phase deposition[11] and so on. Among the above techniques, soft-chemistry-based methods have attracted a great deal of attention from the viewpoint of low-cost, less dependence on specific equipment and easier morphology control.

Like other materials, the properties and performance of TiO_2 are significantly affected by its morphology and structure. A lot of effort has been made to prepare TiO_2 with different architectures to boost its performance in different applications. Among them, mesocrystals, with an ordered arranged hierarchical superstructure, are of great interest.[12,13] TiO_2 mesocrystals are built from TiO_2 nanocrystals with common crystallographic orientation. This structure has been demonstrated to bring the material not only properties associated with individual nanocrystals but also collective properties from the crystallographically ordered assembly, resulting in excellent performance in various applications.[14–16] Taking DSSCs as the example, the high specific surface area from the individual TiO_2 nanoparticles enables a high dye loading; the overall large particle size helps to increase light scattering; the dual pore structure offers improved mass transport for redox-couples; and the structural coherence attributes to long-range electronic connectivity.[17–20] All of these features make TiO_2 mesocrystals promising candidates for the photoanode of DSSCs.

The fabrication of TiO_2 mesocrystals can adopt two main strategies, namely bottom-up and top-down. The bottom-up strategies always include the hydrolysis of Ti sources (such as $TiCl_4$ and tetrabutyl orthotitanate) to form TiO_2 nano-building blocks and the assembly of the nano-building blocks with different templates or driving force.[21] Opposite to this, topotactic transformation has been proposed as a top-down strategy to make mesocrystals.[22–24] In this solid-to-solid process, the products are transformed from a precursor with crystallographic similarity, so they always inherit the overall size and the morphology from the precursor. The morphology control over the precursor material will bring new structural possibilities to the products. In the case of TiO_2, NH_4TiOF_3 has been widely adopted as the topotactic precursor of anatase TiO_2, since the {001} facets of NH_4TiOF_3 and of anatase TiO_2 share a similar Ti pattern.[22] $(NH_4)_2TiOF_4$, with the Ti atom arrangement on its {001} facets similar to the {100} facets of NH_4TiOF_3, was also studied as the precursor of anatase TiO_2, and the stepwise conversion was named as successive topotactic conversion.[25] Other precursor

B. Lei, N. Robertson
School of Chemistry
The University of Edinburgh
Edinburgh EH9 3FJ, UK
E-mail: Neil.Robertson@ed.ac.uk

The ORCID identification number(s) for the author(s) of this article can be found under https://doi.org/10.1002/solr.202200831.

DOI: 10.1002/solr.202200831

materials were also investigated, such as $CaTiO_3$[26] and protonated titanate.[27] However, most work has focused on powder form materials, which means further immobilization steps are needed for applications that require film formation. The transformation from an immobilised precursor is less studied, but would offer a simplified preparation method for functional TiO_2 mesocrystal films.

In this work, we obtained immobilised $(NH_4)_2TiOF_4$ on various substrates for the first time through a soft-chemistry-based method. By applying a thermal successive topotactic transformation, immobilised mesocrystal TiO_2 (imcTiO_2) with exposed {001} facets was prepared via simple sintering processes. Compared with an earlier hydrothermal-based synthesis route,[28] this method provides a higher feasibility to scale up the reaction or control the reaction parameters and thus the geometrical parameters and properties of the products. The materials were characterized by X-ray Diffraction (XRD), Scanning Electron Microscopy (SEM) and Transmission Electron Microscopy (TEM). The properties, formation mechanism and effect from the sintering programmes are discussed in detail. The imcTiO_2 films were applied as the photoanode for DSSCs as a means to illustrate the properties and performance from the new structure. Due to the high surface area, structural coherence and exposed {001} facets of the nano-building-blocks, imcTiO_2 showed an outstanding fill factor (FF) and satisfactory open-circuit voltage (V_{OC}) and short-circuit current density (J_{SC}), compared with commercial TiO_2 nanoparticles (Ti-Nanoxide T/SP, Solaronix). Moreover, an immobilised NH_4TiOF_3 array was also obtained as the stable intermediate of the successive topotactic transformation from the immobilised $(NH_4)_2TiOF_4$, which may attract further future study and interest.

2. Results and Discussion

2.1. Immobilised $(NH_4)_2TiOF_4$ Characterization

After a low-temperature hydrolysis reaction of $(NH_4)_2TiF_6$, immobilised $(NH_4)_2TiOF_4$ was obtained on various types of substrate. **Figure 1**a shows XRD patterns of hydrolysed products on an FTO-$TiCl_4$ substrate with the concentration ratio between $(NH_4)_2TiF_6$ and $(NH_4)O_2CCH_3$ as 0.4:1. The pattern matched well with the reported powder diffraction pattern (PDF) of $(NH_4)_2TiOF_4$ (ICSD 75 405),[29] indicating that phase-pure $(NH_4)_2TiOF_4$ was successfully obtained. Compared with the PDF card or XRD results of powder form $(NH_4)_2TiOF_4$ in literature,[25] the samples on FTO-$TiCl_4$ showed preferred orientation with increased intensities of (020) and (121) and decreased intensity of (101)/(002) ($2\theta = 23.6°$, 28.7° and 16.2° respectively). Since the b-axis of $(NH_4)_2TiOF_4$ is parallel to the elongated axis of the rod-shape particle, this indicates a preferential alignment of rods towards the vertical direction. The reaction was also tested with other substrates like bare FTO, sanded glass and Glass-$TiCl_4$, with XRD of the products shown in Figure S1, Supporting Information, supporting the wide applicability to different substrates. SEM images of $(NH_4)_2TiOF_4$ on FTO-$TiCl_4$ are shown in Figure 1b–d. It can be observed that $(NH_4)_2TiOF_4$ rods with ≈50 μm length and ≈10 μm cross-sectional width formed an immobilised array on each substrate, with the rods

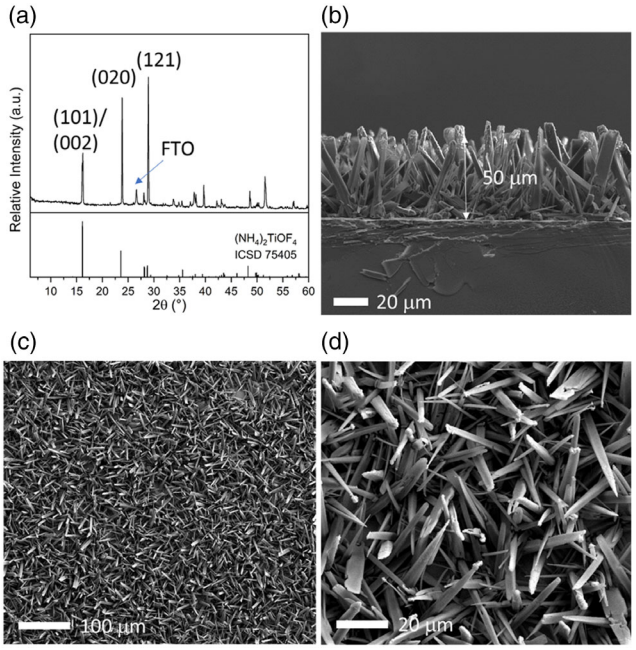

Figure 1. a) XRD and b–d) SEM images of immobilised $(NH_4)_2TiOF_4$ on FTO-$TiCl_4$.

aligned towards the perpendicular consistent with the preferred orientation observed in XRD results. Higher concentrations of $(NH_4)_2TiF_6$ were also tested using FTO-$TiCl_4$ as the substrates (Figure S2 and S3, Supporting Information), which didn't change the crystal phase and preferred orientation of the product but produced immobilised $(NH_4)_2TiF_4$ with larger particle size and larger overall film thickness.

2.2. Immobilised $(NH_4)_2TiOF_4$ Formation Mechanism

The hydrolysis of $(NH_4)_2TiF_6$ with the addition of boric acid (H_3BO_3) has been widely studied and denoted as a liquid phase deposition when TiO_2 powder or thin films were obtained as the product.[11] The main reactions can be represented as follows

$$[TiF_6]^{2-} + nH_2O \rightleftharpoons [TiF_{6-n}(OH)_n]^{2-} + nH^+ + nF^- \quad (1)$$

$$[Ti(OH)_6]^{2-} + 2H^+ \rightleftharpoons TiO_2 \downarrow + 4H_2O \quad (2)$$

$$H_3BO_3 + 4HF \rightleftharpoons H^+ + BF_4^- + 3H_2O \quad (3)$$

In this process, H_3BO_3 works as a fluoride scavenger which promotes the consumption of F^- ions and thus the hydrolysis process. Some studies also used alumina as the scavenger and simultaneously a template for making TiO_2 nanowires and nanotubes.[30] The corresponding reaction has been proposed as

$$Al_2O_3 + 12F^- + 12H^+ \rightleftharpoons 2H_3AlF_6 + 3H_2O \quad (4)$$

NH_4TiOF_3 has been reported as a stable intermediate of the hydrolysis of $(NH_4)_2TiF_6$ following the possible processes[22]

$$[TiF_6]^{2-} + 3H_2O \rightleftharpoons [TiF_3(OH)_3]^{2-} + 3H^+ + 3F^- \quad (5)$$

$$[TiF_3(OH)_3]^{2-} + H^+ + NH_4^+ \rightleftharpoons NH_4TiOF_3 \downarrow + 2H_2O \quad (6)$$

Powder form NH_4TiOF_3 was successfully obtained by adding various surfactants into the reaction to hinder the complete hydrolysis of $[TiF_6]^{2-}$ or using certain concentrations of NH_4OH in H_3BO_3-free reaction to adjust the equilibrium in Equation (1).[14,31,32] Similarly, powder form $(NH_4)_2TiOF_4$ has also been obtained by increasing the concentration of $(NH_4)_2TiF_6$ and NH_4OH in H_3BO_3-free reaction.[25] Possible reactions are shown below

$$[TiF_6]^{2-} + 2H_2O \rightleftharpoons [TiF_4(OH)_2]^{2-} + 2H^+ + 2F^- \quad (7)$$

$$[TiF_4(OH)_2]^{2-} + 2NH_4{}^+ \rightleftharpoons (NH_4)_2TiOF_4 \downarrow + H_2O \quad (8)$$

However, the precipitation process is too fast to induce crystal growth on any substrate. In the work reported here however, by replacing NH_4OH with less basic $(NH_4)O_2CCH_3$, the reaction in Equation (7) may be hindered, so the hydrolysis process will be slowed down. After introducing the substrate material into the reaction, SiO_2 for glass-based substrates, or TiO_2 for $TiCl_4$ pre-treated substrates, will react with F^- according to[33,34]

$$SiO_2 + 6F^- + 4H^+ \rightleftharpoons [SiF_6]^{2-} + 2H_2O \quad (9)$$

$$TiO_2 + 6F^- + 4H^+ \rightleftharpoons [TiF_6]^{2-} + 2H_2O \quad (10)$$

For a static reaction system as employed in this work, the consumption of F^- by the substrate is expected to result in a relatively lower concentration of F^- near the substrates and thus the preferable crystal growth on the substrates, a similar mechanism to the liquid phase deposition of TiO_2 on alumina templates as mentioned above.

2.3. Immobilised TiO_2 Mesocrystals (imcTiO_2) Characterization

The imcTiO_2 was prepared by simply sintering immobilised $(NH_4)_2TiOF_4$ at high temperature in ambient atmosphere, following a successive topotactic transformation strategy.[25] Different sintering temperatures and programmes were tested, with the details and corresponding material names shown in **Figure 2**. For example, S2S600 means sintering the sample at 600 °C for 2 h with a slow heating rate (2 °C min^{-1}) and a slow cooling process within the furnace (≈3 h). In contrast, ultrafast heating and cooling, e.g., F2F600, are used to denote placing the sample in the pre-heated furnace and taking it out right after the dwelling time respectively. From XRD patterns of immobilised samples on Glass-$TiCl_4$ after sintering at 500 °C (Figure S4a, Supporting Information) or 600 °C (**Figure 3**a) with different programmes, all samples were successfully converted to TiO_2 in the anatase phase (ICDD 86-1156). The various peak widths indicate different crystallinity of those samples. The crystallite domain size of each sample was calculated by applying the Scherrer equation to the (101) diffraction peak ($2\theta = 25.3°$) and listed in **Table 1**. It is shown that higher temperature and a faster heating procedure led to bigger crystallite sizes. The cooling process also affected the crystallite size but to a much lesser extent. SEM images are shown in Figure 3 and S4b, Supporting Information. Low magnification SEM image of the sample sintered with S2S600 programme (Figure 3b) shows that after the sintering procedure, the material retained the overall size and shape of the precursor, which is typical for the solid-to-solid topotactic transformation reaction. Higher magnification images (Figure 3c–f, S4b, Supporting Information) show the TiO_2 samples possessed different surface texture, possibly owing to the different TiO_2 crystal growth under different sintering programmes.

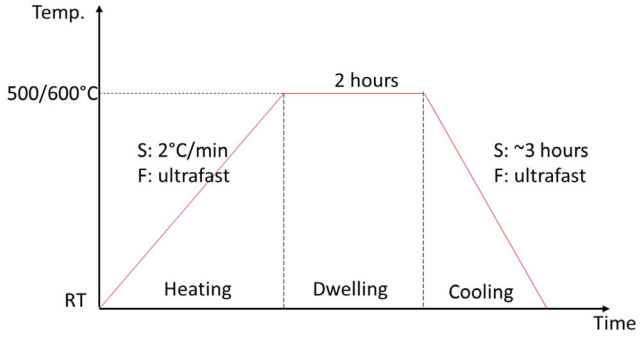

Figure 2. Illustration of the sintering programmes.

More structural information of the imcTiO_2 was given by TEM. All the samples were scratched from the immobilised films and crushed to smaller pieces before the testing. **Figure 4**a shows the image of a crushed fragment of the sample S2S600. Higher magnification image in Figure 4b indicates that the large particle was composed of nanoparticles with a common orientation and with the size around 20 nm, which is consistent with the crystallite size calculated from the XRD result. Selected-Area Electron Diffraction (SAED) was conducted in the circled area shown in Figure 4a and S5a, Supporting Information. Generally, the result possesses a single-crystal like pattern but with distortions, which is a typical feature for mesocrystals.[13] The indexation of the resulted SAED pattern is shown in FigureS5b,c, Supporting Information. Due to the minor rotation of some nanoparticles along the a-axis in the large selected area, there are two sets of single-crystal like patterns which can be indexed to [010] and [01-1] zone respectively. A corresponding HRTEM image for the latter was collected and shown in Figure S5d, Supporting Information. Figure 4c shows the STEM image of one nanoparticle with clear edges and a hexagonal shape, corresponding to the typical [010]-view of an anatase nanoparticle with exposed {001} facets and a truncated bipyramidal shape as shown in the inset of Figure 4c.[35] Based on the thickness (≈13.8 nm) and length (≈24.1 nm) measured via ImageJ, the ratio of the exposed {001} facets of the nanoparticles to the total surface area can be calculated as around 35% (details are given in Supporting Information).

TEM images of the samples under other sintering programmes are also shown (Figure 4d–f, S4c,d, S6, Supporting Information). The common orientation of nanoparticles can be observed for all the samples, confirming the mesocrystal structure of the products from different sintering programmes. The most obvious difference is the particle size, with slower heating progress and lower sintering temperature leading to smaller nanoparticles, also consistent with the order of their average crystalline size obtained from XRD results. The samples from slow heating programme showed smaller size dispersions, which may be the result of the gradually and evenly increased temperature over the samples. The ratio of {001} facets was also calculated for all the other samples and listed in Table S1, Supporting Information. The sintering programme slightly varied the exposure of the {001} facets. Samples from slow heating procedure

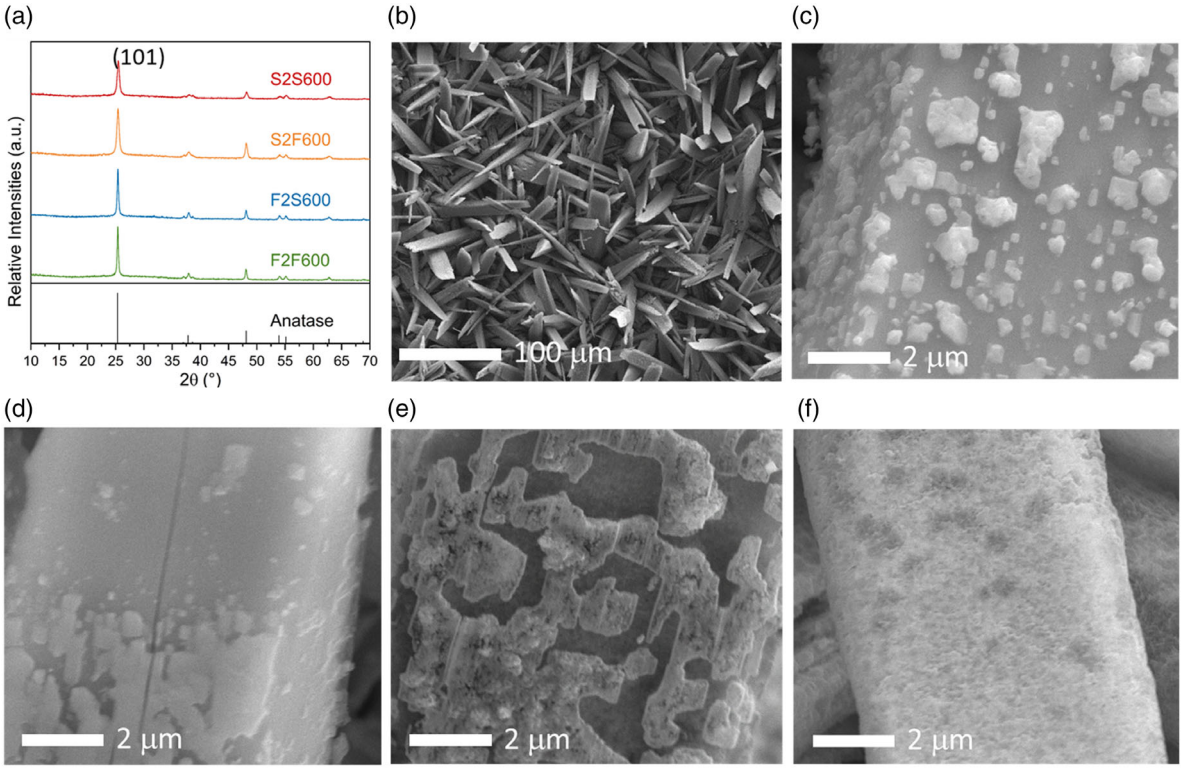

Figure 3. a) XRD of samples sintered at 600 °C with different programme; SEM images of samples sintered at 600 °C under b,c) S2S600, d) S2F600, e) F2S600, and f) F2F600.

Table 1. Comparison of imcTiO$_2$ and commercial reference TiO$_2$ (labelled as T2, ≈8 μm, vide infra) in terms of crystallite size, dye uptake capability, *J*–*V* parameters, trap distribution parameter α and diffusion coefficient β. Mean values ± s.d. for *J*–*V* parameters were calculated based on 4–5 devices for each TiO$_2$.

Sintering Programme	D_{101} [nm]	Dye loading [10^{-7} mol cm^{-2}]	J_{SC} [mA cm^{-2}]	V_{OC} [V]	FF	PCE [%]	α	β
S2S500	13.43	3.34	12.97 (11.55 ± 0.95)	0.70 (0.69 ± 0.00)	0.72 (0.72 ± 0.02)	6.5 (5.7 ± 0.5)	0.26	0.72
S2S600	18.01	2.37	12.27 (11.50 ± 0.53)	0.72 (0.72 ± 0.00)	0.73 (0.74 ± 0.01)	6.4 (6.0 ± 0.3)	0.34	0.64
S2F600	17.75	2.22	12.54 (10.81 ± 1.52)	0.71 (0.71 ± 0.00)	0.72 (0.73 ± 0.01)	6.4 (5.6 ± 0.7)	0.34	0.68
F2S600	28.76	1.21	9.62 (8.96 ± 0.76)	0.74 (0.74 ± 0.01)	0.72 (0.71 ± 0.01)	5.2 (4.7 ± 0.5)	0.22	0.59
F2F600	31.01	1.20	10.34 (9.13 ± 0.87)	0.73 (0.73 ± 0.00)	0.73 (0.72 ± 0.01)	5.5 (4.8 ± 0.5)	0.22	0.58
T2-S2S500	17.8	1.07	13.45 (12.19 ± 1.28)	0.71 (0.71 ± 0.01)	0.70 (0.68 ± 0.01)	6.7 (5.8 ± 0.7)	0.23	0.59
T2-S2S600	22.32	0.90	13.47 (11.93 ± 1.58)	0.73 (0.71 ± 0.01)	0.70 (0.70 ± 0.02)	6.8 (5.9 ± 0.8)	0.28	0.61

showed slightly higher ratio of {001} facets, possibly attributed from the stabilization effect of the more slowly released F^-.[36] Compared with S2S500, S2S600 possessed similar thickness but larger length scales, resulting in a relatively higher ratio of exposed {001} facets, the possible reason and impact of which will be further discussed in next sections.

2.4. Immobilised TiO$_2$ Formation Mechanism

The topotactic transformation conversion from $(NH_4)_2TiOF_4$ to mesocrystal TiO$_2$ has been investigated based on the powder form samples, with NH_4TiOF_3 detected as an intermediate product.[25] This is because $(NH_4)_2TiOF_4$ doesn't have direct crystallographical similarity with anatase but both of them are similar to NH_4TiOF_3. In this work, the intermediate of the conversion from immobilised $(NH_4)_2TiOF_4$ to imcTiO$_2$ was also detected with an immobilised form. The XRD result (**Figure 5**a) of the sample collected after heating the immobilised $(NH_4)_2TiOF_4$ to 250 °C matched well with reported data for NH_4TiOF_3 (ICSD 54-0239), indicating that $(NH_4)_2TiOF_4$ had been converted to NH_4TiOF_3 at this temperature. The SEM images (Figure 5b, S7, Supporting Information) show that the intermediate NH_4TiOF_3 retained the overall morphology of the precursor $(NH_4)_2TiOF_4$ and the rod-shape particles were composed of

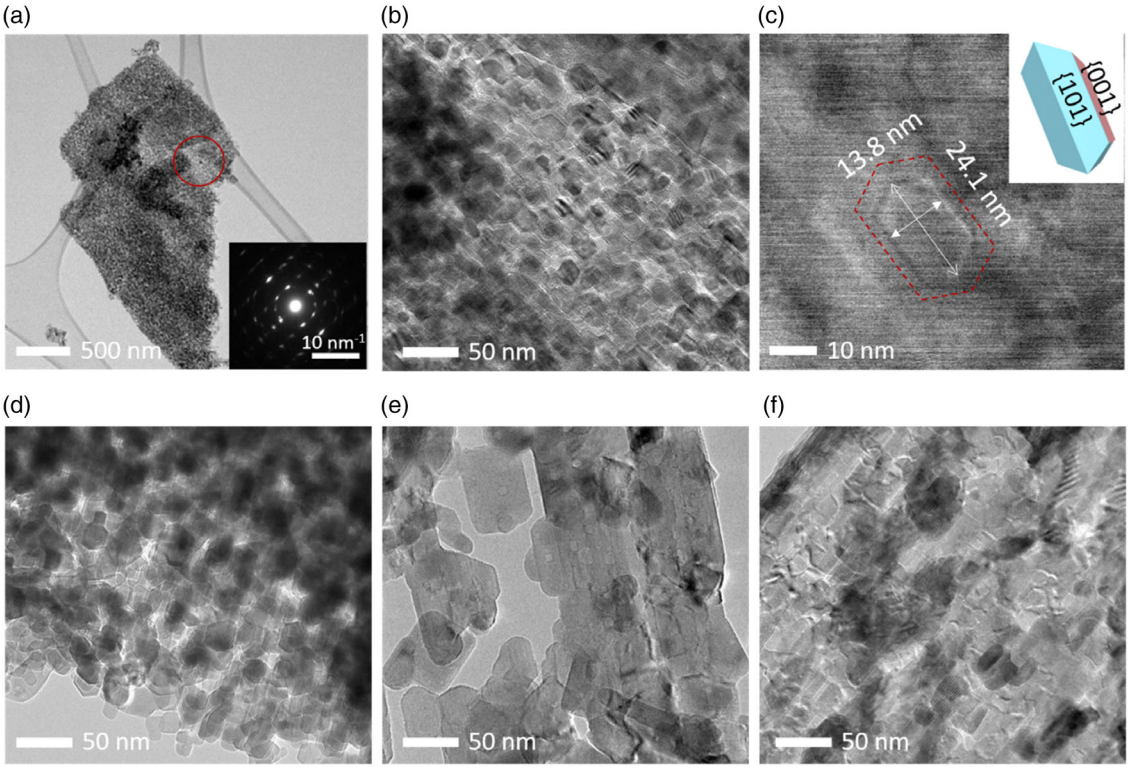

Figure 4. TEM images of samples sintered at 600 °C under a–c) S2S600, d) S2F600, e) F2S600, and f) F2F600. Inset of (a) SAED of the sample sintered at 600 °C under programme S2S600.

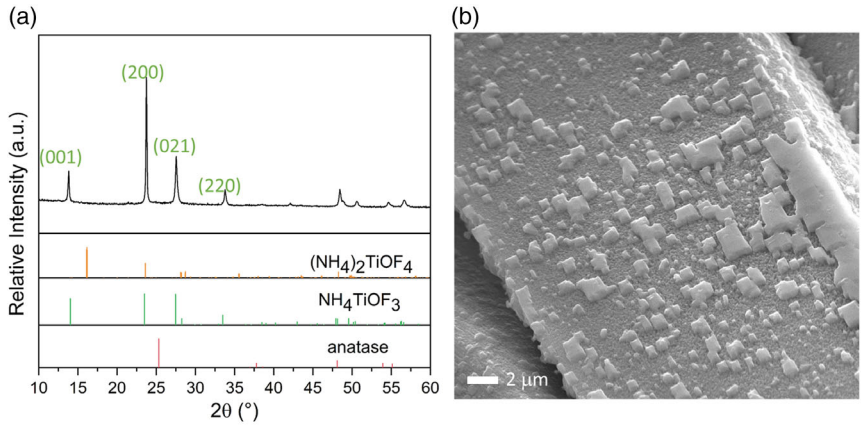

Figure 5. a) XRD and b) SEM image of the sample sintered to 250 °C.

smaller particles with a common orientation, in line with the feature of the topotactic transformation reaction.

The conversion from the intermediate NH_4TiOF_3 to imcTiO_2 occurred between 250 and 280 °C, with the sample collected at 280 °C showing XRD peaks of both (Figure S8a, Supporting Information). Crystallite size of the anatase was calculated as 11.17 nm based on the (101) diffraction peak. The sample collected at 300 °C (Figure S8b, Supporting Information) showed the dominant peaks of anatase phase with slightly increased D_{101} as 13.84 nm, which is close to D_{101} of S2S500 and lower than D_{101} of S2S600. This implies that the conversion started with solid-state nucleation and the nanosized nucleus grew bigger with increasing temperature. During the topotactic conversion from NH_4TiOF_3 to TiO_2 mesocrystal, shrinkage and rearrangement of the crystal structure occurs more likely along [001] direction of anatase due to the lattice mismatch along this direction and the removal of the interlamellar NH_4^+, while {001} facets remain less changed as the topotactic conversion templates. This may contribute to an anisotropic crystal growth with the increasing temperature via either Ostwald ripening or oriented attachment of the crystallographically aligned nanoparticles, explaining the increased ratio of {001} facet at a higher sintering temperature.[37,38]

2.5. DSSCs Application

In this work we chose DSSCs as an example of the versatile applications of TiO_2 films to investigate the performance of imcTiO_2 with exposed {001} facets. A traditional sandwich-type configuration was used with LEG4 dye as the sensitizer, I^-/I_3^- redox couple the electrolyte, and Pt coated FTO the counter electrode. Photoanodes were all prepared on FTO-$TiCl_4$ to minimize the possible charge recombination at the FTO/electrolyte interface.[39] We firstly compared different concentration ratios between $(NH_4)_2TiF_6$ and $(NH_4)O_2CCH_3$ for preparing $(NH_4)_2TiOF_4$ precursor. Figure S9, Supporting Information, shows that 0.5:1 and 0.6:1 led to higher J_{SC} and power conversion efficiency (PCE) than 0.4:1, which could be mainly because of the improved dye uptake capability (See Table S2, Supporting Information) from more densely packed larger imcTiO_2 rods. The reusibility of the container for the synthesis was tested by recording the *J–V* parameters of the devices based on the precursor material synthesized in a container that have been reused for different times. According to Figure S10, Supporting Information, when the concentration ratio between $(NH_4)_2TiF_6$ and $(NH_4)O_2CCH_3$ was 0.6:1, there was no significant variance of any *J–V* parameters, even after the container was reused for 5 times. This indicates the better reproducibility of high-quality films and reusibility of the container with a higher concentration of $(NH_4)_2TiF_6$. Based on this, the ratio 0.6:1 was used for further comparisons.

Figure 6 shows the *J–V* curves of DSSCs based on imcTiO_2 sintered at different temperatures or with different programmes, compared with reference devices using 2 layers of commercially-available transparent TiO_2 as photoanodes (≈8 μm, Ti-Nanooxide T/SP, Solaronix, denoted as T2 followed by the heating regime). It can be observed that devices based on imcTiO_2 show slightly higher hysteresis than commercial TiO_2 based cells, which could possibly arise from their different electrolyte ion diffusion or total trap densities, where further investigation is required.[40,41]

Important parameters, J_{SC}, V_{OC}, FF and PCE, were extracted from the reverse scans and are compared in Table 1. The cell based on imcTiO_2 annealed at 500 °C with the programme S2S500 showed comparable PCE (5.7 ± 0.5%) to devices based on 2 layers of reference TiO_2 (5.8 ± 0.7%). The reference cells with more layers of TiO_2 showed increased J_{SC} therefore slightly higher PCE (Figure S11, Table S2, Supporting Information), but are not considered in further comparison because of the relatively complicated screen-printing processes. When both imcTiO_2 and reference TiO_2 were prepared at higher temperature (600 °C), the cells based on both achieved increased V_{OC} and FF. The J_{SC} from different cells varies too much to be compared, but the average for high-temperature imcTiO_2 samples showed a smaller decrease compared with reference TiO_2. Overall, higher sintering temperature led to improved PCE for imcTiO_2 (from 5.7 ± 0.5% to 6.0 ± 0.3%), and the effect was more significant than TiO_2 from the commercial paste (5.8 ± 0.7% vs 5.9 ± 0.8%).

Dye loading is always considered as an important factor affecting the J_{SC} of DSSCs. The dye loading of imcTiO_2 and reference TiO_2 prepared with different sintering programmes were tested and listed in Table 1. The imcTiO_2 showed around 2 times higher dye loading than screen-printed commercial TiO_2 (T2) under the same annealing programme, because of the much thicker film obtained from the hydrolysis reaction (80 vs 8 μm, estimated from cross-sectional SEM, Figure S3 and 12, Supporting Information), and the open structure of the immobilised TiO_2 arrays versus compact packing of nanoparticles in screen-printed TiO_2. Higher annealing temperature reduced the dye loading of each TiO_2, possibly because of the decreased surface area which can be indicated by the increased crystallite size (shown in Table 1), and supported by the particle sizes of different imcTiO_2 calculated from TEM results (Table S1, Supporting Information). It is worth noting that widely adopted Brunauer-Emmett-Teller (BET) surface area analysis was not used in this work considering the inconvenience for film samples. It was also observed that the change in the dye pickup didn't lead to significant change in J_{SC} for devices, indicating the possible impact from other aspects, which will be discussed in the next section.

The imcTiO_2 sintered at 600 °C with different programmes also shows different J–V performances (Figure 6b). Generally, the heating processes impact the overall PCE more than the cooling processes, with slow heating enabling higher dye loading therefore higher J_{SC} for the devices, consistent with their structural difference resulting from the sintering programmes. The different cooling procedures did not make much difference on

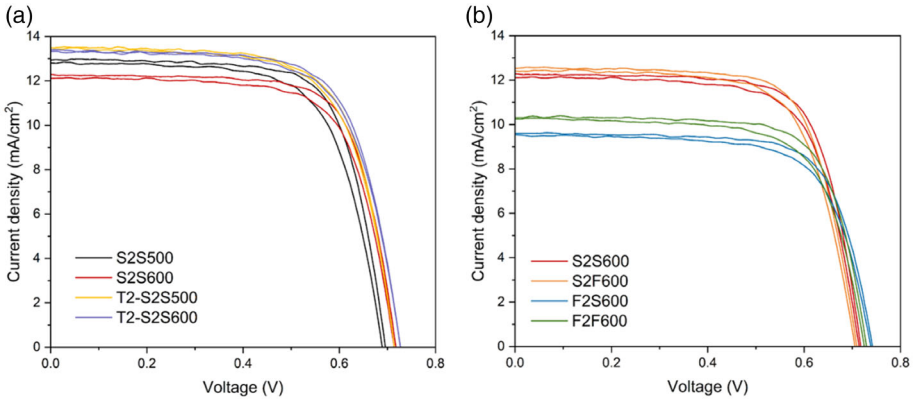

Figure 6. *J–V* curves of devices based on immobilised TiO_2 sintered under different programme and reference TiO_2 (labelled as T2, ≈8 μm). Both forward scans (from J_{SC} to V_{OC}) and reverse scans (from V_{OC} to J_{SC}) are shown with reverse scans always giving higher PCE and other performance parameters.

the cell performance, which also indicated the undamaged film quality or substrates after the fast cooling procedure. This was also supported by the recorded incident photon-to-current conversion efficiency (IPCE) spectra and integrated J_{SC} from IPCE spectra (Figure S13, Supporting Information), showing higher IPCE maximum from devices based on slow heating programmes. Higher V_{OC} was obtained from cells based on F2S600 and F2F600, but the larger nanoparticle sizes of those samples resulted in a lower surface area, leading to much lower dye loading and J_{SC} of those cells.

It is worth noting that devices based on imcTiO$_2$ show generally high FF. The champion cell based on S2S600 achieved 0.74 ± 0.01, an impressive value surpassing most of the reports on DSSCs. FF is an important parameter which is strongly related to the ease of charge transport in the device.[42] The general high FF of imcTiO$_2$-based DSSCs implies efficient charge transport in these cells, which is very likely due to the strong adhesion of TiO$_2$ films based on direct growth synthesis route, structural coherence of the mesocrystals and the common orientation of the nano-building-blocks.[43]

Electrochemical impedance spectroscopy (EIS) was measured to provide information on the charge transfer and charge transport mechanisms in the DSSCs with different TiO$_2$ as photoanodes. Nyquist plots were recorded at open circuit conditions under white LED illumination. Important electron transfer parameters were extracted from the EIS data by applying a transmission line equivalent circuit model.[44] Figure S14, Supporting Information, shows the example Nyquist plot of the cell S2S600 under a bias of 0.7 V and the corresponding fitting result. One of the most important parameters is the chemical capacitance (C_μ) at the sensitized TiO$_2$/electrolyte interface, which can reflect the variation of the density of sub-bandgap traps. **Figure 7**a,d show C_μ of devices based on different TiO$_2$ as a function of applied potential, which increases exponentially with increasing voltage, following the relationship[45]

$$C_\mu = C_0 \exp\left(\frac{\alpha q V}{k_B T}\right) \tag{11}$$

$$C_0 = L(1-p)\alpha \frac{q^2 N_t}{k_B T} \exp\left[\frac{\alpha(E_{redox} - E_c)}{k_B T}\right] \tag{12}$$

where N_t is the total number of trap states below the conduction band, L the film thickness, p the porosity of the film, q the elementary charge, k_B the Boltzmann constant and (E_{redox}–E_c) the energy difference between redox potential of electrolyte and conduction band of TiO$_2$. α is a parameter describing the depth of trap distribution below the conduction band, which can be extracted from the slope of lnC_μ plots.[46] It is a complicated parameter that can be affected by the size, morphology, structural order and other factors of the material.[47,48] By comparing α of different TiO$_2$ (Table 1), it can be found that higher temperature and slower heating rate resulted in larger α which means a shallower trap distribution. Compared with commercial nanoparticles TiO$_2$, imcTiO$_2$ exhibited higher α when they were sintered under the same conditions. As a consequence, S2S600 sample offered the largest α among all the samples therefore the shallowest trap distribution, which would be beneficial for charge collection via the trap-detrap process.[49] This may be

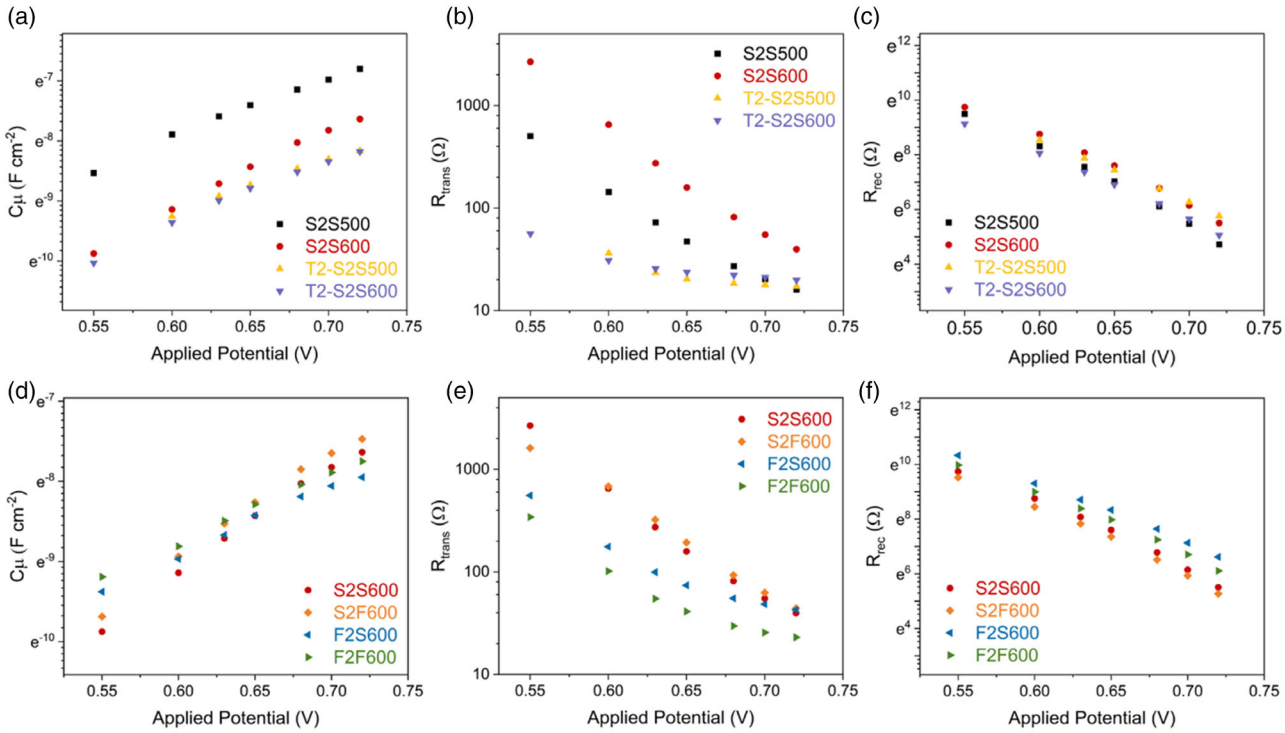

Figure 7. a,d) C_μ, b,e) R_{trans}, and c,f) R_{rec} of DSSCs based on immobilised TiO$_2$ under different sintering programmes or reference TiO$_2$, plotted versus applied potential. S2S600 was repeated for an easier comparison.

the reason for the similar J_{SC} of S2S600-based cells compared with S2S500, despite having relatively lower dye uptake.

From Equation (11) and (12), it can be seen that the geometrical dimensions, namely the thickness (L) and porosity (p), significantly affect the value of C_μ. This explains the higher C_μ of imcTiO$_2$ based cells compared with devices using commercial TiO$_2$, which gave thinner films but more densely packed nanoparticles. The total number of trap states (N_t) also influences the overall capacitance. Higher sintering temperature and faster heating rate always result in higher crystallite size and less trap density at grain boundaries or amorphous domains between the crystallites within the TiO$_2$ films, therefore a smaller N_t.[50] However, in the case of imcTiO$_2$, this also brings a different ratio of {001} facets, which possess a higher conduction band (CB) minimum than {101} facets.[51] Therefore, the gaps between E_c and E_{redox} for different imcTiO$_2$ become different. Overall, the relatively low CB of S2S500 among all the imcTiO$_2$ samples and highest N_t due to the smallest crystallinity led to the highest C_μ of devices based on S2S500. For samples sintered at 600 °C under different programmes, parameters offset each other and resulted in similar C_μ values.

The CB shift of imcTiO$_2$ can be also reflected by the electron transport resistance (R_{trans}), which can be expressed as[44]

$$R_{trans} = R_{t,0} \exp\left[-\frac{E_F - E_c}{k_B T}\right] \tag{13}$$

with $R_{t,0}$ a constant relating to the geometrical dimensions of TiO$_2$ and E_F the position of the quasi-Fermi level in TiO$_2$ that can be adjusted by the applied potential. The plots of R_{trans} of DSSCs based on different TiO$_2$ versus the applied potential are given in Figure 7b,e. The different geometrical dimensions of imcTiO$_2$ and commercial TiO$_2$ led to the variance of the R_{trans}. Higher temperature increased the R_{trans} of imcTiO$_2$ at fixed E_F, which is likely due to the higher ratio of {001} facets and the correspondingly higher E_c (further from E_F). This structural variation is not expected for the commercial TiO$_2$, so a smaller difference in R_{trans} of different commercial TiO$_2$ is observed. As discussed before, faster heating rate for preparing imcTiO$_2$ photoanode reduces the ratio of exposed {001} facets, in line with the smaller R_{trans} of F2S600 and F2F600 at fixed potential in Figure 7e.

R_{trans} reflects how effectively the electron moves through the TiO$_2$ network. In order to further study the electron transport kinetics of the DSSCs based on different TiO$_2$, R_{trans} was also plotted versus the total electron concentration (n) that can be calculated from C_μ by the following equation[52]

$$n = \frac{k_B T}{\alpha q^2 L} C_\mu \tag{14}$$

The plots are given in Figure S15, Supporting Information. The plateauing of R_{trans} for commercial TiO$_2$ at high electron concentration is because of the limitation of the transmission line model for determining R_{trans} under such conditions. The data suggest the commercial TiO$_2$ shows higher R_{trans} than imcTiO$_2$ at high total electron concentration. For imcTiO$_2$, higher sintering temperature and faster heating rate resulted in larger crystallite size and less crystal boundaries, which increased the electron transport kinetics and thus a smaller R_{trans} at fixed charge density. Trap distribution also affects the electron transport. For example, the shallowest trap distribution of S2S600 contributed to the lower R_{trans} at the same total electron concentration compared with S2S500, and reduced the gap between S2S600 and F2F600 or F2S600 in the R_{trans} versus n plot.

The recombination resistance (R_{rec}) at the TiO$_2$/dye/electrolyte interface was also plotted versus applied potential in Figure 7c,f. The order of the R_{rec} for devices based on different TiO$_2$ is consistent with the order of their V_{OC} under 1 sun illumination. The relationship between R_{rec} and the applied potential has been given as[45]

$$R_{rec} = R_{r,0} \exp\left[-\frac{\beta q V}{k_B T}\right] \tag{15}$$

$$R_{r,0} = \frac{\sqrt{\pi \lambda k_B T}}{q^2 L \alpha k_r c_{ox} N_s} \exp\left[\frac{\alpha(E_c - E_{redox})}{k_B T} + \frac{\lambda}{4 k_B T}\right] \tag{16}$$

where λ and c_{ox} are the reorganization energy and concentration of acceptor species (I_3^-), both of which are constant in this work since the same electrolyte was used for all devices. k_r is the rate constant accounting for recombination kinetics. β is the transfer coefficient that can be extracted from the slope of lnR_{rec} plots (Table 1). The β value ($\beta < 1$ for DSSCs) describes the contribution of surface states or conduction band to the charge recombination, with higher value corresponding to less contribution from surface states.[53] Except for S2S500, the β value for DSSCs based on different TiO$_2$ showed a general correlation with the trap distribution parameter α. More specifically, the shallow trap distribution reduces the charge transfer through traps, which is consistent with the observations in other works.[53,54] N_s, the total number of surface states, is another parameter affecting the charge recombination and is related to the surface area of TiO$_2$ photoanodes. The order of the R_{rec} for devices based on different TiO$_2$ matches well with the order of crystallinity of TiO$_2$ estimated from XRD results, so opposite to the order of their surface area, consistent with the relationship given by Equation (16).

R_{rec} versus n plots also help to study the recombination kinetics of the devices. According to Figure S16, Supporting Information, cells based on imcTiO$_2$ have faster recombination kinetics compared with reference TiO$_2$ sintered at the same condition. Higher sintering temperature and slower heating rate resulted in faster recombination at the fixed charge density. The recombination kinetics are closely connected to the trap distribution and concentration under the conduction band of TiO$_2$. The overall recombination performance must have been affected by other parameters since the overall R_{rec} versus potential and V_{OC} of cells showed different trends, especially comparing S2S600, S2S500 and reference TiO$_2$. In addition to the aforementioned β and N_s, the conduction band position (E_C) of TiO$_2$ also determines the charge recombination. A higher conduction band of TiO$_2$ and a wider gap between the conduction band and quasi-Fermi level will reduce the chance of the recombination, denoted as larger (E_c–E_{redox}) in Equation (16). As a consequence, S2S600 with the higher conduction band than S2S500 and reference TiO$_2$ showed relatively higher overall R_{rec} at fixed applied potential. However, the much closer conduction band of imcTiO$_2$ sintered at different programmes couldn't offset the contribution

from the trap distribution, leading to a similar trend of R_{rec} at the same charge concentration and at the fixed potential, as well as V_{OC} of cells based on these imcTiO$_2$.

In summary, compared with commercial TiO$_2$, imcTiO$_2$ under the same sintering conditions possesses in general faster charge transport kinetics due to the unique mesocrystal structural features and reasonable recombination resistance attributed to the exposed {001} facets. Sintering conditions have more effect on the structure and hence electronic performance of imcTiO$_2$ compared with their typical effect on commercial titania. A faster sintering procedure results in larger crystallite size and less trap density, which is beneficial to the faster electron transport kinetics and slower charge recombination. However, shallower trap distribution and higher ratio of {001} facets from a slow sintering procedure reduce the performance variance. There is generally excellent electron transport for all of the imcTiO$_2$ materials.

3. Conclusion

Herein we demonstrated for the first time a soft-solution-chemistry-based method for the preparation of immobilised $(NH_4)_2TiOF_4$, which can be selectively converted to immobilised NH_4TiOF_3 or to immobilised TiO$_2$ mesocrystal arrays by thermal topotactic conversion. This method is applicable to all the SiO$_2$ based substrates or SiO$_2$/TiO$_2$ treated substrates, satisfying the requirement of various applications. The topotactic conversion reaction opens up new possibilities for the structure of immobilised TiO$_2$. The example application of DSSCs proved the high quality and excellent performance of the obtained imcTiO$_2$ associated with the combination of the mesocrystal structure, the exposed {001} facets and the immobilisation. We believe that future modification of the imcTiO$_2$ and the cell configuration can produce DSSCs with higher performance. And this new approach to immobilised mesocrystal materials has the potential to also bring unique features to other application areas such as water treatment, UV-detectors, energy storage and H_2 production.

4. Experimental Section

Preparation of Substrate Materials: Fluorine-doped tin oxide (FTO)-coated glass substrates (TEC7, Merck), glass slides (Thermo Scientific) were used as substrates with or without pre-treatments. They were cut into pieces of size 1.5 cm × 2 cm and glass slides were sanded by a sand paper prior to the cleaning process. To clean the substrates, they were sonicated in 2 vol% Hellmanex detergent solution for 30 min, DI water for 15 min, ethanol for 15 min and dried with hot air and treated by UV/ozone for 20 min. Some substrates were pre-treated by a $TiCl_4$ aqueous solution (40 mM) at 70 °C for 30 min, followed by a water rinse and a heat treatment at 500 °C for 30 min, and labelled as FTO-$TiCl_4$ or Glass-$TiCl_4$.

Preparation of Immobilised $(NH_4)_2TiOF_4$: Immobilised $(NH_4)_2TiOF_4$ was prepared by immersing substrates in a mixed solution of $(NH_4)_2TiF_6$ and $(NH_4)O_2CCH_3$. Typically, × gram of $(NH_4)_2TiF_6$ (Acros Organics) was dissolved in H_2O (3.6 mL) and stirred at 50 °C in a 30 mL glass container. $(NH_4)O_2CCH_3$ (400 µL, 10 M) was pipetted into $(NH_4)_2TiF_6$ solution under magnetic stirring. The value of × was 0.317, 0.396 and 0.475 in order to obtain a concentration ratio of $(NH_4)_2TiF_6$ and $(NH_4)O_2CCH_3$ to be 0.4:1, 0.5:1 and 0.6:1. After stirring the solution for 5 min, the stirrer bar was taken out and the substrate material was immersed in the solution with the active layer facing up. After 24 h, the substrates with white coating were taken out, rinsed gently with water and ethanol, and dried with hot air.

Preparation of Immobilised TiO$_2$ Mesocrystals (imcTiO$_2$): ImcTiO$_2$ were prepared by annealing the immobilised $(NH_4)_2TiOF_4$ precursor with different programmes. Specifically, an S2S procedure means sintering the sample to a desired temperature for 2 h with a slow heating rate of 2 °C min^{-1} and cooling it down to room temperature naturally in the furnace which takes around 3 h; To conduct F2S sintering programme, the sample was placed in the furnace after the furnace had been pre-heated to the desired temperature and cooled down in the furnace (≈3 h to near room temperature); S2F and F2F have the same heating programme as S2S and F2S respectively but a faster cooling by taking the sample out of the furnace right after 2 h of sintering. The sintering temperature is denoted by a numeric suffix.

Characterization: X-Ray diffraction (XRD) was carried out on a Bruker D2 PHASER using Cu Kα radiation. Surface and cross-sectional SEM images of samples were collected using a ZEISS SIGMA Field Emission SEM, operated in SE2 mode with a 10 kV accelerating voltage. To prepare specimens for cross-section analysis, the substrates were scored before the reaction and were broken along the score after preparation of films and adhered on a stub with the cross section facing up. TEM and SAED were carried out using a FEI Titan Themis microscope.

Working Electrode: Immobilised $(NH_4)_2TiOF_4$ on FTO-$TiCl_4$ was scratched to obtain a 5 mm × 5 mm pattern, followed by the annealing procedure as described above. A post-treatment was carried out by immersing the annealed sample in a $TiCl_4$ aqueous solution (40 mM) at 70 °C for 30 min, followed by rinsing with water, drying in air and annealing at 500 °C for 30 min. The films were immersed in a dye bath while they were still warm (80–100 °C) and were left at room temperature for 20 h. The dye bath contained 0.2 mM LEG4 (Dyenamo) in acetonitrile/tert-butanol (1:1, v/v).

Commercial nano-particle TiO$_2$ paste (Ti-Nanoxide T/SP, Solaronix) was screen-printed on FTO-$TiCl_4$ through a polyester screen (mesh count: 90) with a 0.2827 cm^2 (D = 6 mm) circular area. The thickness of obtained TiO$_2$ films was controlled by adjusting the number of printed layers. The printed films were annealed with S2S500 and S2S600 procedure and labelled as Tx2S500 and TxS2S600 with x the number of printed layers. The post-treatment and dye soaking of reference TiO$_2$ from commercial paste followed the procedure for imcTiO$_2$.

Counter Electrodes: FTO glass was cut into pieces of size 1.5 cm × 2 cm and was sonicated in 2 vol% Hellmanex detergent solution, water, HCl (0.1 M in ethanol) and ethanol for 15 min sequentially. A platinum precursor paste (Solaronix Platisol-T) was doctor-bladed on the substrates, followed by annealing at 450 °C for 15 min to obtain a platinized FTO glass electrode.

Cell Assembly: The working electrode and counter electrode were clamped together with FTO side facing each other. A UV-curing sealant (TB3035B, Threebond) was applied on edges and solidified by UV torch. An Iodolyte HI-30 electrolyte solution (Solaronix) was injected through a pre-drilled hole in the counter electrode by vacuum back filling and the hole was then sealed with Surlyn cover and a microscope coverslip.

Solar Cell Testing: Photocurrent density-voltage (J–V) curves were recorded on an Autolab potentiostat (Metrohm) with class AAA SLB300A solar simulator (Sciencetech) as the light source. The light intensity was calibrated to AM1.5G using a silicon reference cell. The active area of the solar cell was fixed with a black metal mask with a circular aperture of 0.0707 cm^2 (d = 3 mm). The frequency-modulated electrochemical impedance was recorded with a similar setup to that of the J–V measurements. The frequency range was set to 1 MHz to 0.05 Hz with an AC voltage amplitude of 10 mV. The measurements were performed under white LED illumination with adjustable intensity. The plots were fitted using the ZView (Scribner Associates) software. Incident photon-to-current conversion efficiency (IPCE) was recorded with a photo-spectrometer setup (Bentham PVE300) by illuminating the solar cell with a modulated monochromatic light (Xenon and quartz halogen lamps) through 1.85 mm slit. The incident light was calibrated with a reference Silicon photodiode and the spectral resolution was set to 2 nm.

Supporting Information

Supporting Information is available from the Wiley Online Library or from the author.

Acknowledgements

The authors thank Dr Aruna Ivaturi and Dr Arivazhagan Valluvar Oli for assistance with IPCE measurements in University of Strathclyde; Dr Aaron Naden for TEM measurements in the University of St. Andrews; and Dr Nicola Cayzer for help with the SEM images acquisition. B.L. gratefully acknowledges the China Scholarship Council and The University of Edinburgh for a PhD scholarship.

Conflict of Interest

The authors declare no conflict of interest.

Data Availability Statement

The data that support the findings of this study are available from the corresponding author upon reasonable request.

Keywords

dye-sensitized solar cells, electrochemical impedance spectroscopy, immobilization, mesocrystals, titanium dioxide

Received: September 9, 2022
Revised: October 30, 2022
Published online:

[1] S. Franz, H. Arab, G. L. Chiarello, M. Bestetti, E. Selli, *Adv. Energy Mater.* **2020**, *10*, 2000652.
[2] H. Wei, E. F. Rodriguez, A. F. Hollenkamp, A. I. Bhatt, D. Chen, R. A. Caruso, *Adv. Funct. Mater.* **2017**, *27*, 1703270.
[3] Z. Zheng, F. Zhuge, Y. Wang, J. Zhang, L. Gan, X. Zhou, H. Li, T. Zhai, *Adv. Funct. Mater.* **2017**, *27*, 1703115.
[4] A. H. Mamaghani, F. Haghighat, C. S. Lee, *J. Photochem. Photobiol., A* **2019**, *378*, 156.
[5] S. K. Dhungel, J. G. Park, *Renewable Energy* **2010**, *35*, 2776.
[6] S. Ito, T. N. Murakami, P. Comte, P. Liska, C. Grätzel, M. K. Nazeeruddin, M. Grätzel, *Thin Solid Films* **2008**, *516*, 4613.
[7] J. Singh, S. A. Khan, J. Shah, R. K. Kotnala, S. Mohapatra, *Appl. Surf. Sci.* **2017**, *422*, 953.
[8] N. Rausch, E. P. Burte, *J. Electrochem. Soc.* **1993**, *140*, 145.
[9] M. Qorbani, O. Khajehdehi, A. Sabbah, N. Naseri, *ChemSusChem* **2019**, *12*, 4064.
[10] Y. Chen, D. D. Dionysiou, *Appl. Catal., B* **2006**, *69*, 24.
[11] S. Deki, Y. Aoi, O. Hiroi, A. Kajinami, *Chem. Lett.* **1996**, *25*, 433.
[12] H. Cölfen, M. Antonietti, *Angew. Chem., Int. Ed.* **2005**, *44*, 5576.
[13] L. Zhou, P. O'Brien, *Small* **2008**, *4*, 1566.
[14] Y. Guo, H. Li, J. Chen, X. Wu, L. Zhou, *J. Mater. Chem. A* **2014**, *2*, 19589.
[15] H. You, Q. Wu, J. Li, S. He, X. Li, X. Yang, J. Yang, Y. Meng, S. Tong, M. Wu, *CrystEngComm* **2017**, *19*, 2456.
[16] M. Di, Y. Li, H. Wang, Y. Rui, W. Jia, Q. Zhang, *Electrochim. Acta* **2018**, *261*, 365.
[17] B. Lei, A. V. Oli, A. Ivaturi, N. Robertson, *Sustainable Energy Fuels* **2022**, *6*, 502.
[18] L.-P. Heiniger, F. Giordano, T. Moehl, M. Grätzel, L. Heiniger, F. Giordano, T. Moehl, M. Grätzel, *Adv. Energy Mater.* **2014**, *4*, 1400168.
[19] E. J. W. Crossland, N. Noel, V. Sivaram, T. Leijtens, J. A. Alexander-Webber, H. J. Snaith, *Nature* **2013**, *495*, 215.
[20] F. Xie, G. Dong, K. Wu, Y. Li, M. Wei, S. Du, *Chem. Phys. Lett.* **2020**, *739*, 136996.
[21] B. Zhang, S. Cao, M. Du, X. Ye, Y. Wang, J. Ye, *Catalysts* **2019**, *9*, 91.
[22] L. Zhou, D. Smyth-Boyle, P. O'Brien, *J. Am. Chem. Soc.* **2008**, *130*, 1309.
[23] T. Shinagawa, M. Watanabe, J. Tani, M. Chigane, *Cryst. Growth Des.* **2017**, *17*, 3826.
[24] X. Y. Kong, T. Tong, B.-J. Ng, J. Low, T. H. Zeng, A. R. Mohamed, J. Yu, S.-P. Chai, *ACS Appl. Mater. Interfaces* **2020**, *12*, 26991.
[25] B. Lei, Y. Guo, H. Xie, J. Chen, X. Li, Y. Wu, L. Zhou, *Cryst. Growth Des.* **2019**, *19*, 5460.
[26] Y. H. Wu, Y. F. Cao, Z. Z. Fu, B. X. Lei, Z. F. Sun, *Adv. Powder Technol.* **2021**, *32*, 186.
[27] D. Hu, W. Zhang, Y. Tanaka, N. Kusunose, Y. Peng, Q. Feng, *Cryst. Growth Des.* **2015**, *15*, 1214.
[28] Y. Zhang, J. Cai, Y. Ma, L. Qi, *Nano Res.* **2017**, *10*, 2610.
[29] J. Patarin, F. Marcuccilli-Hoffner, H. Kessler, P. Daniels, *Eur. J. Solid State Inorg. Chem.* **1994**, *31*, 501.
[30] A. Sadeghzadeh Attar, Z. Hassani, *J. Mater. Sci. Technol.* **2015**, *31*, 828.
[31] M. Inoguchi, M. Afzaal, N. Tanaka, P. O'Brien, *J. Mater. Chem.* **2012**, *22*, 25123.
[32] Y. Liu, Y. Zhang, H. Li, J. Wang, *Cryst. Growth Des.* **2012**, *12*, 2625.
[33] S. Verhaverbeke, I. Teerlinck, C. Vinckier, G. Stevens, R. Cartuyvels, M. M. Heyns, *J. Electrochem. Soc.* **1994**, *141*, 2852.
[34] G. Wu, J. Wang, D. F. Thomas, A. Chen, *Langmuir* **2008**, *24*, 3503.
[35] J. Pan, G. Liu, G. Q. Lu, H. M. Cheng, *Angew. Chem., Int. Ed.* **2011**, *50*, 2133.
[36] H. G. Yang, C. H. Sun, S. Z. Qiao, J. Zou, G. Liu, S. C. Smith, H. M. Cheng, G. Q. Lu, *Nature* **2008**, *453*, 638.
[37] J. Chen, B. Lei, H. Xie, L. Zhou, S. Wang, *Chem. Mater.* **2017**, *29*, 7653.
[38] L. Zhou, J. Chen, C. Ji, L. Zhou, P. O'Brien, *CrystEngComm* **2013**, *15*, 5012.
[39] L. Vesce, R. Riccitelli, G. Soscia, T. M. Brown, A. Di Carlo, A. Reale, *J. Non-Cryst. Solids* **2010**, *356*, 1958.
[40] F. Wu, X. Li, Y. Tong, T. Zhang, *J. Power Sources* **2017**, *342*, 704.
[41] S. Sarker, H. W. Seo, Y. K. Jin, K. S. Lee, M. Lee, D. M. Kim, *Electrochim. Acta* **2015**, *182*, 493.
[42] C. Altinkaya, A. Atli, A. Atilgan, K. Salimi, A. Yildiz, *Int. J. Energy Res.* **2020**, *44*, 3160.
[43] X. Sheng, D. He, J. Yang, K. Zhu, X. Feng, *Nano Lett.* **2014**, *14*, 1848.
[44] F. Fabregat-Santiago, J. Bisquert, G. Garcia-Belmonte, G. Boschloo, A. Hagfeldt, *Sol. Energy Mater. Sol. Cells* **2005**, *87*, 117.
[45] S. R. Raga, E. M. Barea, F. Fabregat-Santiago, *J. Phys. Chem. Lett.* **2012**, *3*, 1629.
[46] J. A. Anta, F. Casanueva, G. Oskam, *J. Phys. Chem. B* **2006**, *110*, 5372.
[47] F. Nunzi, E. Mosconi, L. Storchi, E. Ronca, A. Selloni, M. Grätzel, F. De Angelis, *Energy Environ. Sci.* **2013**, *6*, 1221.
[48] F. Nunzi, L. Storchi, M. Manca, R. Giannuzzi, G. Gigli, F. De Angelis, *ACS Appl. Mater. Interfaces* **2014**, *6*, 2471.
[49] Q. Wang, Z. Zhang, S. M. Zakeeruddin, M. Grätzel, *J. Phys. Chem. C* **2008**, *112*, 7084.
[50] J. Lin, M. Guo, C. T. Yip, W. Lu, G. Zhang, X. Liu, L. Zhou, X. Chen, H. Huang, *Adv. Funct. Mater.* **2013**, *23*, 5952.

[51] N. Martsinovich, A. Troisi, *Phys. Chem. Chem. Phys.* **2012**, *14*, 13392.
[52] P. R. F. Barnes, K. Miettunen, X. Li, A. Y. Anderson, T. Bessho, M. Gratzel, B. C. O'Regan, *Adv. Mater.* **2013**, *25*, 1881.
[53] Q. Wang, S. Ito, M. Grätzel, F. Fabregat-Santiago, I. Mora-Seró, J. Bisquert, B. Takeru, H. Imai, *J. Phys. Chem. B* **2006**, *110*, 25210.
[54] J. Bisquert, A. Zaban, M. Greenshtein, I. Mora-Seró, *J. Am. Chem. Soc.* **2004**, *126*, 13550.